



## Triboelectric potential tuned dual-gate IGZO transistor for versatile sensory device

Feixia Tan<sup>a,b</sup>, Yao Xiong<sup>b,c</sup>, Jinran Yu<sup>b,c</sup>, Yifei Wang<sup>b,c</sup>, Yonghai Li<sup>a,b</sup>, Yichen Wei<sup>a,b</sup>, Jia Sun<sup>d</sup>, Xiaoyin Xie<sup>e,\*</sup>, Qijun Sun<sup>a,b,c,\*\*</sup>, Zhong Lin Wang<sup>b,c,f,\*\*</sup>

<sup>a</sup> Center on Nanoenergy Research, School of Physical Science and Technology, Guangxi University, Nanning 530004, PR China

<sup>b</sup> Beijing Institute of Nanoenergy and Nanosystems, Chinese Academy of Sciences, Beijing 101400, PR China

<sup>c</sup> School of Nanoscience and Technology, University of Chinese Academy of Sciences, Beijing 100049, PR China

<sup>d</sup> School of Physics and Electronics, Central South University, Changsha 410083, PR China

<sup>e</sup> School of Chemistry and Chemical Engineering, Hubei Polytechnic University, Huangshi 435003, China

<sup>f</sup> School of Materials Science and Engineering, Georgia Institute of Technology, Atlanta, GA 30332-0245, United States

### ARTICLE INFO

#### Keywords:

Triboelectric potential  
Tribotronics  
Dual-gate transistor  
Multifunctional sensor  
Artificial synapse

### ABSTRACT

Sophisticated intelligent interactive system calls for energy-efficient strategy to multifunctional versatile sensory devices. Triboelectric potential derived from triboelectric nanogenerators (TENGs) can be readily utilized to integrate with dual-gate transistor and implement multiple sensing applications. Here, we present a device-level versatile sensory platform based on triboelectric potential tuned dual-gate IGZO transistors with a common bottom gate and an air-dielectric top gate, which can be used as multifunctional sensors (including distance/pressure/optical sensor and artificial photonic synapse). The versatile transistor device can be readily driven by the triboelectric potential and associated with mechanical displacement as a highly sensitive distance sensor. According to the capacitance change of air-dielectric top gate upon external pressure and the intrinsic photo-conductivity of IGZO channel, it also integrates a pressure and optical sensor. As the existence of oxygen-deficiency-related persistent photocurrent characteristics in IGZO channel, versatile transistor device is also facile to imitate the biological synaptic behaviors by light pulse. Assisted with synergistic triboelectric potential modulation, the updated synaptic weights can be readily used for image edge detection. The proposed device-level sensory platform has great potentials in versatile and multifunctional intelligent sensors, interactive robotic skin, image recognition and neuromorphic chip.

## 1. Introduction

Emerging and widespread applications of intelligent manufacturing, Internet of Things, in-memory sensing/computing and artificial intelligence urgently call for energy-efficient strategy to multifunctional versatile sensory devices. [1–12] Some promising solutions have been raised to integrate energy-harvesting components (e.g., piezoelectric/pyroelectric/triboelectric harvesters, [13–15] solar cells [16], and biofuel cells) with functional devices to realize self-powered sensation, communication, instruction, etc. Regarding to arbitrary/distributed/facile feasibility of self-powered systems, [17,18] a convenient method is required to convert ubiquitous and low-frequency mechanical energy in ambient environments (or touch-interactive scenarios) into

electricity to power/trigger/modulate the target devices. [19,20] Triboelectric effect is a common and inevitable phenomenon accompanying in daily life when two different materials contact each other. The triboelectric potential (or triboelectricity) can also be readily produced by contact electrification via triboelectric nanogenerators (TENGs), [21] which is driven by Maxwell's displacement current [22] and originated from electrostatic induction under periodic (or irregular) mechanical contact-separation actions. The collected triboelectricity has been extensively utilized to power portable electronics, [23–25] induce plasma in atmospheric environment, [26] drive self-powered sensors, [27,28] probe interface charges, [29] etc. The triboelectric potential is also encouraged to power/modulate conventional field effect transistors (FETs) [30,31] and unconventional ion-controlled/electro

\* Corresponding author.

\*\* Corresponding authors at: Beijing Institute of Nanoenergy and Nanosystems, Chinese Academy of Sciences, Beijing 101400, PR China  
E-mail addresses: [xyxie@hbpu.edu.cn](mailto:xyxie@hbpu.edu.cn) (X. Xie), [sunqijun@binn.cas.cn](mailto:sunqijun@binn.cas.cn) (Q. Sun), [zhong.wang@mse.gatech.edu](mailto:zhong.wang@mse.gatech.edu) (Z.L. Wang).

<https://doi.org/10.1016/j.nanoen.2021.106617>

Received 31 July 2021; Received in revised form 25 September 2021; Accepted 8 October 2021

Available online 11 October 2021

2211-2855/© 2021 Elsevier Ltd. All rights reserved.

chemical/neuromorphic transistors, [32–35] inspiring diversified applications in active-matrix E-skin, [36–38] mechano-phonic neuromorphic devices, [39] artificial afferents, [40] etc. Until now, the integration of versatile functionalities into a unit tribotronic transistor is still lack of investigations, but highly demanded toward upcoming era of artificial intelligent Internet of Things and smart robotics.

FET is an excellent sensory platform for various sensing applications, e.g., pressure sensors with microstructured dielectrics [41,42] or air dielectrics, [43–46] tactile sensor based on interdigitated electrodes, [47] strain sensor triggered by piezopotential, [48] and temperature/humidity/optical sensors with various channel materials. [49–51] Besides, facile interface engineering [52,53] or surface modification [54] is available to achieve transistor-type practical chemical/biological sensors. Architecture engineering (e.g., extended-gate or dual-gate design) is also an efficient way to expand limited architecture space of

a transistor device and develop multifunctional sensors. [55] Dual-gate architecture is specifically beneficial for the transistor-type sensor with additional multiparameter sensation (e.g., drain current, threshold voltage, on/off ratio) and tunable sensitivity due to the superposition of dual-gating effects. [27] As triboelectric potential can be readily utilized to power/modulate the transistor device, it is possible to integrate TENG with dual-gate transistor and broaden the sensing scenarios to implement multifunctional applications. Accordingly, triboelectric potential tuned dual-gate device may mainly cover the following lightspots for versatile sensations: (i) mechanical displacement derived triboelectric potential gating for distance sensor; (ii) integration of a second air-gap dielectric layer to introduce pressure sensing; (iii) optional high-mobility indium-gallium-zinc oxide (IGZO) channel for optical sensor and potential artificial photonic synapse. [56,57].

Here, we present a device-level versatile sensory platform based on

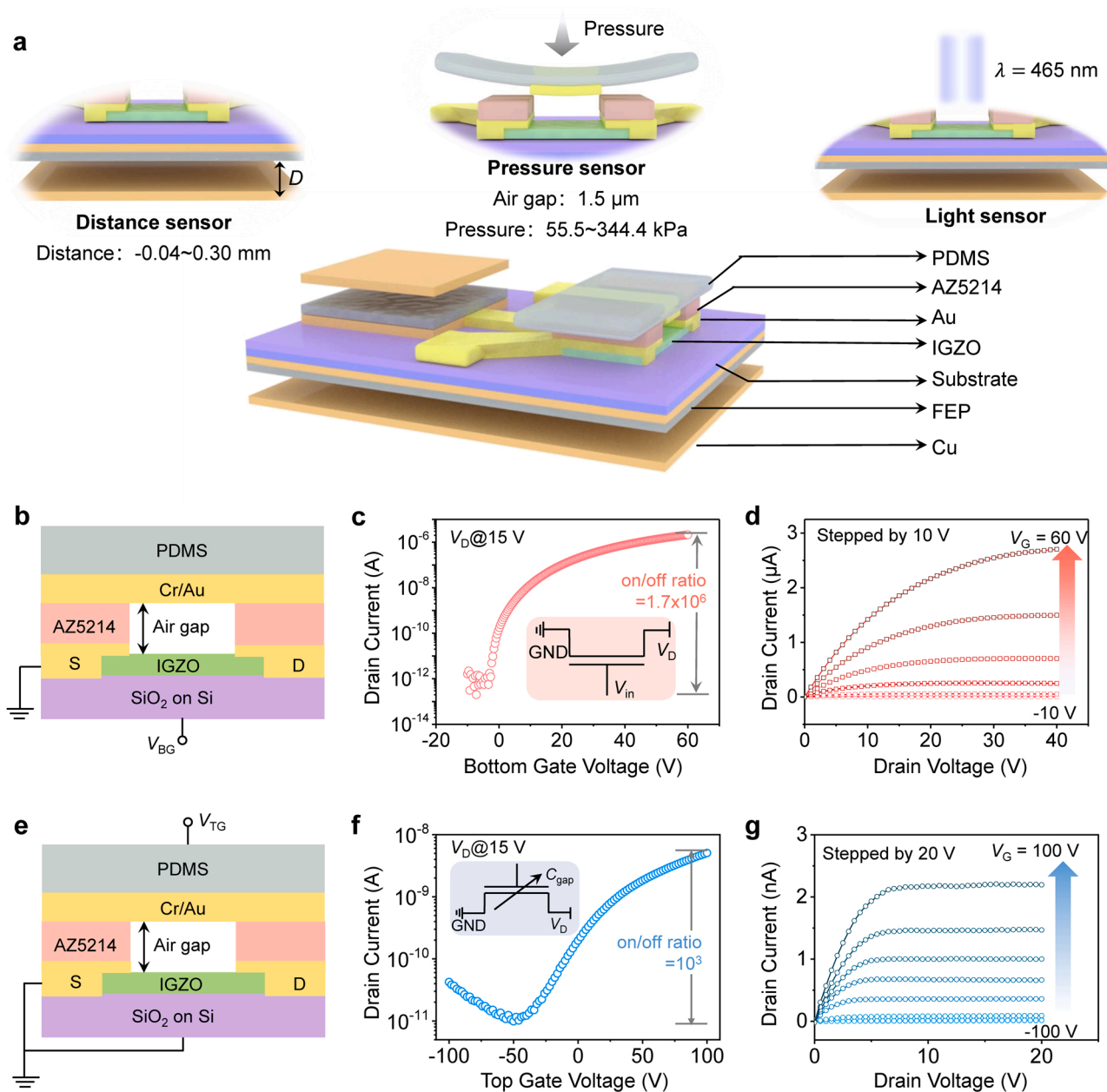


**Fig. 1.** (a) Schematic diagram of the versatile sensory platform based on triboelectric potential tuned dual-gate IGZO transistor. (b) The schematic of tribotronic dual-gate IGZO transistor modulated by bottom gate. (c) The typical transfer characteristics of IGZO transistor gated from bottom gate. Inset is the circuit diagram. (d) The output characteristics of IGZO transistor gated from bottom gate. (e) The schematic of dual-gate IGZO transistor modulated by top gate. (f) Typical transfer characteristics and (g) output characteristics of IGZO transistor modulated by top gate. Inset is the circuit diagram.

triboelectric potential tuned dual-gate IGZO transistors with a common SiO<sub>2</sub>/Si bottom gate and an air-dielectric top gate. The device-level versatile platform can be used as multifunctional sensors, including distance sensor, pressure sensor, optical sensor, and artificial photonic synapse. Specially, the device-level versatile platform (or versatile transistor device) can be readily driven by the triboelectric potential from TENG bottom gate and associated with mechanical displacement as a distance sensor. It shows a sensitivity of  $2.05 \times 10^5 \text{ mm}^{-1}$  in small displacement region ( $-0.04$  to  $0.16 \text{ mm}$ ) and a higher sensitivity of  $15.73 \times 10^5 \text{ mm}^{-1}$  in large displacement region ( $0.16$ – $0.3 \text{ mm}$ ). According to the capacitance change of air-dielectric top gate upon external pressure, it also integrates a sensitive pressure sensor, which can response to small pressures ranging from  $55$  to  $344.4 \text{ kPa}$  and possess short response time ( $\sim 120 \text{ ms}$ ). The combined optical sensor represents a responsivity of  $10^5 \text{ A/W}$ , which works relying on the excited electrons induced by ionized oxygen vacancies in IGZO channel. Based on the optical sensor with oxygen-deficiency-related persistent photocurrent characteristics, an artificial photonic synapse is also achieved to imitate the biological synaptic behaviors including excitatory postsynaptic current, short-term and long-term plasticity. The updated synaptic weights by triboelectric potential tuned photonic postsynaptic current can be readily used for image edge detection. Notably, driven by the triboelectric potential associated with mechanical displacement, the versatile transistor can realize synergetic sensations with distance sensing as a “bridge” to link other two types of sensing, i.e., synergetic pressure/optical sensing upon mechanical displacement modulation (or triboelectric potential modulation). The demonstrated device-level sensory platform is qualified to be utilized in versatile and multifunctional sensors, image analysis and neuromorphic technology in near future.

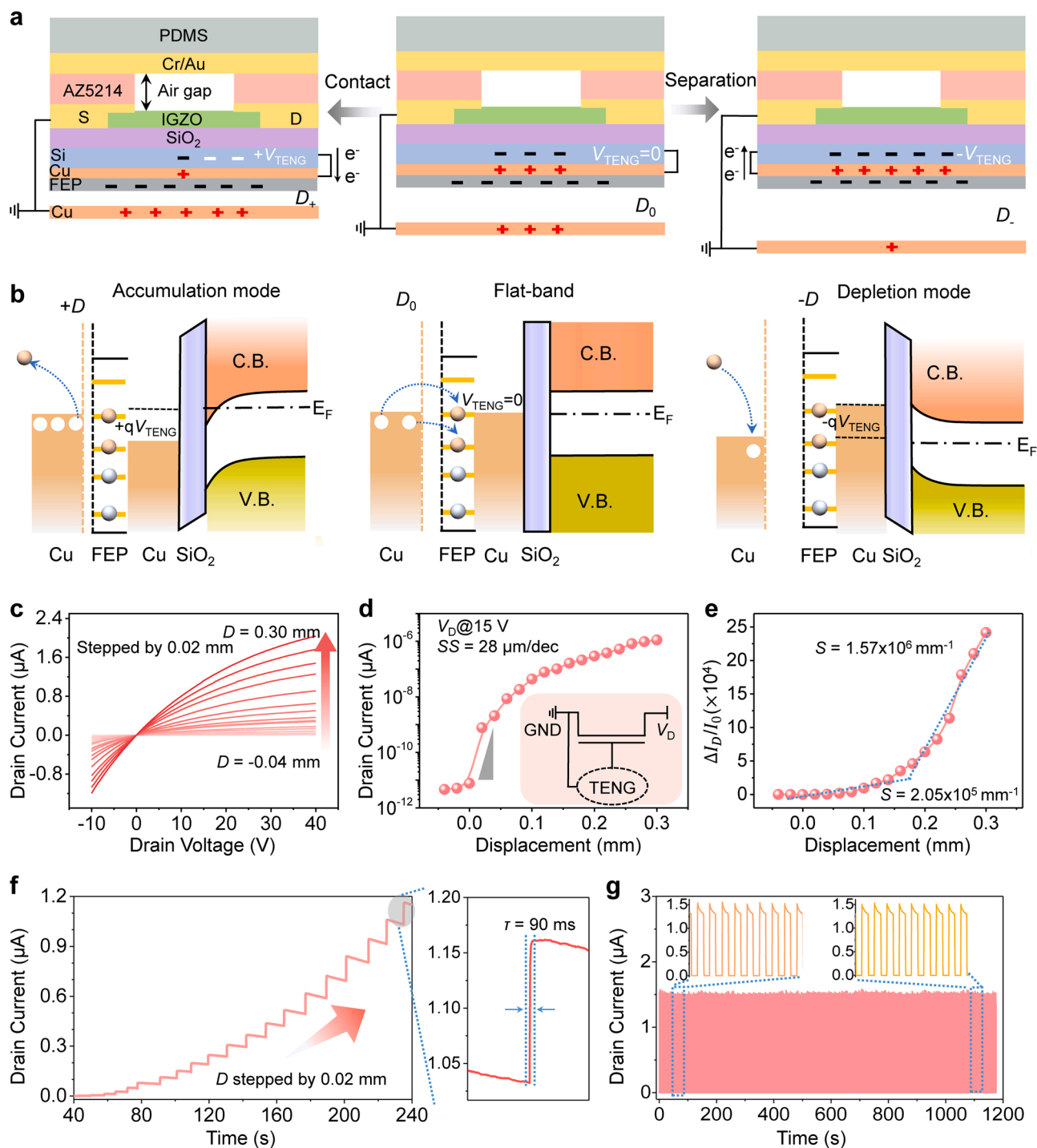
## 2. Results and discussion

Fig. 1a shows the schematic illustration of the versatile sensory platform based on tribotronic dual-gate IGZO transistor. It includes a bottom gate driven by an integrated TENG component and a top gate via air dielectrics. Solution processed IGZO prepared on the SiO<sub>2</sub>/Si wafer is utilized as the channel material due to its high charge carrier mobility and low-temperature processing conditions. [58] The integrated TENG component is composed of Cu/fluorinated ethylene propylene (FEP)/Cu (Cu/FEP/Cu) and mounted on the bottom of SiO<sub>2</sub>/Si wafer. Compared with conventional IGZO transistor, the tribotronic dual-gate IGZO device uses triboelectric potential ( $V_{\text{TENG}}$ ) induced by mechanical displacement ( $D$ ) to control the drain-source current ( $I_{\text{D}}$ ) instead of applied gate voltage ( $V_{\text{G}}$ ). To work as a versatile sensory platform, the tribotronic device possesses the following advantages: (i) as the coupled triboelectric potential  $V_{\text{TENG}}$  is directly related with the distance between Cu and FEP/Cu, the integrated TENG gating component can also be used as a displacement sensor, associating external  $D$  with  $I_{\text{D}}$ ; (ii) air-dielectric top gate constructed by employing typical supporting beam structure promises the device to work as a pressure sensor, through which the applied force ( $F$ ) can induce the variations of air-gap height and corresponding air-dielectric capacitance change to correlate with  $I_{\text{D}}$ ; (iii) IGZO transistor is ready to work as a photodetector and highly sensitive to UV/visible light. (iv) as the photoconductivity is originated from oxygen-deficiency-related defects (which permit a persistent photocurrent), the device is also promising to be applied as an artificial photonic synapse to investigate spatiotemporal correlations of light pulses. Corresponding fabrication process of the versatile sensory device is shown in Fig. S1.

Fig. 1b shows the sectional view of dual-gate IGZO transistor gated from bottom Si gate. A typical positive photoresist (AZ5214, MicroChem) serves as the spacer to support the elastic polydimethylsiloxane (PDMS) mold with Cr/Au electrode, forming the air-gap top gate dielectrics of  $\sim 1.5 \mu\text{m}$ . When the bottom gate voltage ( $V_{\text{BG}}$ ) is applied from  $-10$ – $60 \text{ V}$  at a constant drain voltage of  $15 \text{ V}$  ( $V_{\text{D}} = 15 \text{ V}$ ),  $I_{\text{D}}$

increases from  $2.1 \text{ pA}$  to  $2.08 \mu\text{A}$ , with current on/off ratio ( $I_{\text{on}}/I_{\text{off}}$ ) and the threshold voltage ( $V_{\text{T}}$ ) at  $1.7 \times 10^6$  and  $0 \text{ V}$ , respectively (Fig. 1c). Inset is the circuit diagram of the IGZO dual-gate device. Fig. 1d displays the typical output characteristics ( $I_{\text{D}}-V_{\text{D}}$ ) with  $V_{\text{BG}}$  applied from  $-10$ – $60 \text{ V}$  stepped by  $10 \text{ V}$ . The  $I_{\text{D}}$  increases from  $27 \text{ pA}$  to  $2.7 \mu\text{A}$  at a  $V_{\text{D}}$  of  $40 \text{ V}$ . The  $I_{\text{D}}$  shows a linear dependence in the lower  $V_{\text{D}}$  region ( $V_{\text{D}} < 10 \text{ V}$ ) and a gradually saturated trend at higher  $V_{\text{D}}$ . The output characteristics indicate an increment trend of the channel conductance with the increased  $V_{\text{BG}}$ . Fig. 1e displays sectional view of dual-gate transistor gated from top air dielectrics. The bottom gate is grounded with the source electrode to avoid capacitive coupling. Figs. 1f and 1g represent the typical transfer characteristics and output characteristics of the dual-gate IGZO transistors driven by the applied top gate voltage ( $V_{\text{TG}}$ ), respectively. With  $V_{\text{TG}}$  sweeping from  $-100$ – $100 \text{ V}$ ,  $I_{\text{D}}$  increases from  $4.8 \text{ pA}$  to  $5.05 \text{ nA}$  with  $I_{\text{on}}/I_{\text{off}}$  and  $V_{\text{T}}$  at  $1 \times 10^3$  and  $25 \text{ V}$ , respectively (Fig. 1f). For the output performance, with  $V_{\text{TG}}$  increased from  $-100$ – $100 \text{ V}$ ,  $I_{\text{D}}$  increases from  $34 \text{ pA}$  to  $2.1 \text{ nA}$  at  $V_{\text{D}}$  of  $15 \text{ V}$ . Similarly, the  $I_{\text{D}}-V_{\text{D}}$  characteristics also show an increment trend of channel conductance with the increased  $V_{\text{TG}}$ . Notably, the  $I_{\text{D}}$  driven by  $V_{\text{BG}}$  is over two orders of magnitude higher than that driven by  $V_{\text{TG}}$  under the same test environment. This could be explained by the capacitive coupling in the dual-gate device. Fig. S2a shows the schematic illustration of the dual-gate capacitive coupling, equivalent to a circuit diagram of two series capacitors (top-gate capacitance  $C_{\text{TG}}$  and back-gate capacitance  $C_{\text{BG}}$ ) connected in parallel with one capacitor (coupling capacitance between back and top gates,  $C_{\text{BT}}$ ). Due to the low permittivity of air dielectrics, the capacitance  $C_{\text{BG}} > C_{\text{BT}} \gg C_{\text{TG}}$ . When the device is tested by sweeping  $V_{\text{BG}}$  with top gate electrode disconnected to ground, the effective back-gate capacitance  $C_{\text{BG-eff}} = C_{\text{BG}} + (C_{\text{TG}}^{-1} + C_{\text{BT}}^{-1})^{-1} < C_{\text{BG}} + C_{\text{TG}}$ . By contrast, when the device is tested by sweeping  $V_{\text{TG}}$  with back-gate electrode disconnected to ground, the effective top-gate capacitance  $C_{\text{TG-eff}} = C_{\text{TG}} + (C_{\text{BG}}^{-1} + C_{\text{BT}}^{-1})^{-1} < C_{\text{TG}} + C_{\text{BT}}$ . Accordingly, the transfer curve under  $V_{\text{BG}}$  sweeping with top gate disconnected shows the highest  $I_{\text{D}}$  compared with other two situations (Fig. S2b). In the case of  $I_{\text{D}}$  under  $V_{\text{BG}}$  sweeping with top gate electrode grounding or dis-grounding (Fig. S2c), the two transfer curves show no significant differences. The above results indicate that the air-dielectric top gating can be readily influenced by grounding/disconnecting bottom gate due to the capacitive coupling effect (more discussions in Supporting Information).

The tribotronic dual-gate IGZO transistor is driven by the integrated TENG component, in which  $V_{\text{G}}$  is replaced by the triboelectric potential ( $V_{\text{TENG}}$ ) induced by the contact-separation between Cu and FEP/Cu friction layers. In order to fully turn off the tribotronic device, an equivalent negative  $V_{\text{G}}$  (i.e.,  $-V_{\text{TENG}}$ ) is required to deplete the IGZO channel by presetting an initial relative distance between two friction layers (denoted as  $D_0$  with  $V_{\text{TENG}} = 0 \text{ V}$ , middle panel of Fig. 2a). In this way, the integrated TENG component can implement both separation and contact actions toward the vertical direction to SiO<sub>2</sub>/Si wafer. When the mobile Cu electrode approaches FEP/Cu friction layer (left panel of Fig. 2a), the integrated TENG can couple  $+V_{\text{TENG}}$  to the IGZO transistor, equivalent to applying  $+V_{\text{G}}$ . When Cu electrode is separated from FEP/Cu friction layer (right panel of Fig. 2a), the stepped mechanical displacement (defined as  $D_-$ ) can induce relevant  $-V_{\text{TENG}}$  from  $0$  to  $-20 \text{ V}$ , equivalent to applying  $-V_{\text{G}}$ . The working principle of the tribotronic dual-gate IGZO transistor is explained as follows. At the preset initial state with relative displacement  $D_0$  (middle panel of Fig. 2b), the electrostatically induced triboelectric charges on Cu and FEP/Cu friction layers are released by grounding operation. This state is to set the initial  $V_{\text{TENG}} = 0 \text{ V}$ , delivering no gating effect on the IGZO channel. When the Cu electrode approaches FEP/Cu friction layer from the initial position  $D_0$  (defined as  $D_+$ , left panel of Fig. 2b), negative charges will be induced on FEP film, leaving positive charges transferred to SiO<sub>2</sub>/Si wafer through Cu electrode and coupling  $+V_{\text{TENG}}$  to the IGZO transistor. In this state, electrons are induced in the IGZO channel and the device



**Fig. 2.** Distance sensor based on tribotronic dual-gate IGZO transistor. (a) Working mechanism for the tribotronic dual-gate IGZO transistor. (b) Schematic illustration of corresponding band diagram in different states. (c) The output characteristics of tribotronic dual-gate IGZO transistor. (d) The transfer characteristic of tribotronic dual-gate IGZO transistor (Inset is the circuit diagram). (e) Sensitivity of the distance sensor. (f) Real time displacement detection. Inset is the extracted response time. (g) Stability test for displacement sensing.

works in the accumulation mode. In contrast, when Cu electrode separates from the FEP/Cu, the electrostatically induced negative charges can't be restricted on FEP and transfer to the transistor gate, coupling  $-V_{TENG}$  to the IGZO transistor (right panel of Fig. 2b). In this state, electrons are depleted in the IGZO channel and the device is turned off. Notably, the initial relative distance  $D_0$  can be optional with variable values, which is selected in proper range to deliver enough equivalent  $V_G$  to accumulate or deplete IGZO channel. At the  $D_0$  position, there is a grounding process to release the initially induced triboelectric charges,

which is equivalent to applying  $V_{TENG} = 0$  V to the transistor. Thus, it is applicable to implement  $D+$  or  $D-$  to the integrated TENG component so as to apply either positive or negative  $V_{TENG}$  (i.e., equivalent  $V_G$ ) to the IGZO channel.

With displacement  $D$  varying from  $-0.1$ – $0.3$  mm (stepped by  $0.02$  mm), the coupled  $V_{TENG}$  can change from  $-20$ – $60$  V (Fig. S3), which is sufficient to drive the dual-gate IGZO device according to the transfer curve in Fig. 1c. The output performance of tribotronic IGZO transistor is shown in Fig. 2c, representing a typical increment tendency

of  $I_D$  with  $D$  increased from  $-0.04$ – $0.3$  mm stepped by  $0.02$  mm. As shown in Fig. 2d, the triboelectric potential derived transfer characteristics display that  $I_D$  increases from  $4.2$  pA to  $1.1$   $\mu$ A with  $D$  swept from  $-0.04$ – $0.3$  mm. The  $I_{on}/I_{off}$  ratio reaches  $\sim 2.6 \times 10^5$ , indicating the coupled triboelectric potential can efficiently gate the IGZO transistor. To further quantify the gating process, we evaluate the  $I_D$  variation for one order of magnitude by TENG displacement in the subthreshold region, which can be considered as a figure of merits of the triboelectric potential tuned transistor and defined as tribotronic subthreshold swing ( $SS_t$ ,  $SS_t = \partial(D)/\partial(\log(I_D))$ ). With  $I_D$  varied from  $10^{-12}$  to  $10^{-9}$  A in the subthreshold region, the  $SS_t$  is estimated to be  $28$   $\mu$ m/dec (Fig. S4). The measured tribotronic output and transfer characteristics in Figs. 2c and 2d are consistent with the electrical properties of IGZO FET in Figs. 1c and 1d, demonstrating the excellent feasibility of triboelectric potential gating. According to the transfer characteristics in Fig. 2d,  $I_D$  shows a bijective function with TENG displacement  $D$ , qualifying the back-gate tribotronic transistor to work as a distance sensor. The sensitivity of the distance sensor can be defined as  $(I_D - I_0)/I_0 / D$ , where  $I_0$  is the initial drain current without TENG gating. It can be extracted from the slope of the curve as shown in Fig. 2e, representing typical two-stage sensing region. The sensitivity is evaluated to be  $2.05 \times 10^5$   $\text{mm}^{-1}$  in small displacement region ( $< 0.16$  mm) and  $15.73 \times 10^5$   $\text{mm}^{-1}$  in large displacement region ( $> 0.16$  mm), respectively. As shown in Fig. 2f,  $I_D$

shows a real-time stepwise increment from  $10$  pA to  $1.16$   $\mu$ A according to the increased  $D$  from  $-0.1$ – $0.3$  mm stepped by  $0.02$  mm. Inset shows the response time ( $\tau$ ) estimated to be as fast as  $\sim 90$  ms under the test by applying external  $D$  with a mechanical linear motor. Fig. 2g shows the stability characterization for distance sensing. The measured  $I_D$  can be maintained stable at  $1.2$   $\mu$ A upon the periodic TENG displacement from  $-0.1$ – $0.3$  mm for over 400 cycles. The excellent stability of the distance sensor is attributed to well-controlled  $I_D$  according to the available real-time  $D$  sweeping (from  $-0.1$  m to  $0.3$  mm, Fig. S5a) and extremely stable output of the integrated TENG component (Fig. S5b).

Air-dielectric FET possesses clean interface between the channel and dielectrics, which can be readily used as pressure or tactile sensor due to its good electrical properties, high sensitivity and reliability. When pressure is applied on the air-dielectric top gate constructed with an elastic mold, the height variation of air gap will lead to the capacitance change and corresponding  $I_D$  change. Based on the versatile sensory device, the top-gate air-dielectric pressure sensing can be combined with triboelectric potential gating to achieve a novel pressure sensor with additional tuning function by mechanical displacement. To achieve the triboelectric potential tuned air-dielectric IGZO device, an extended top-gate electrode is prepared on the  $\text{SiO}_2/\text{Si}$  wafer together with source-drain electrodes. Then the PDMS elastic mold with deposited top gate electrode is laminated on the IGZO channel and spaced by the

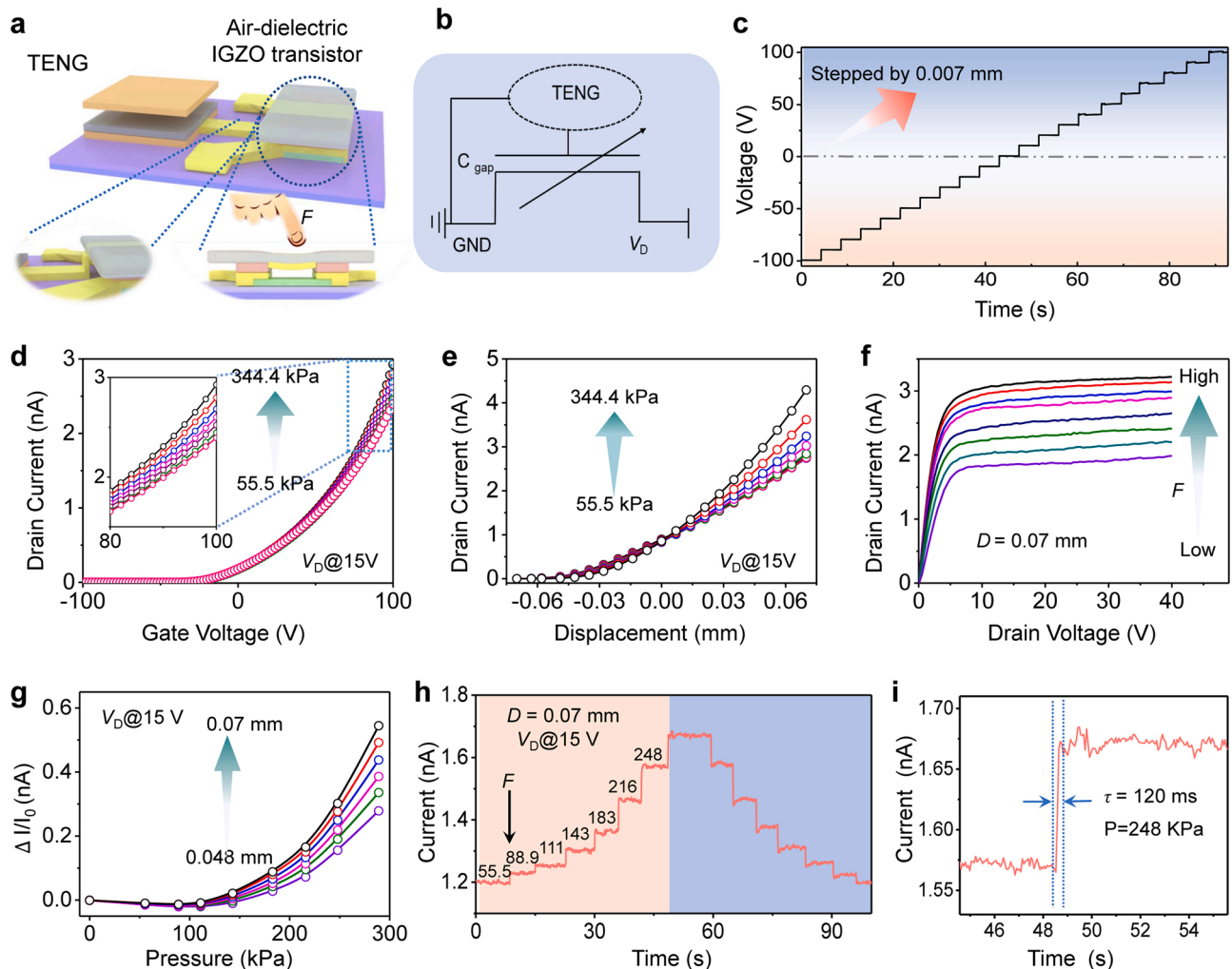


Fig. 3. Pressure sensor based on tribotronic IGZO transistor with air dielectrics. (a) Schematic diagram of pressure sensor based on tribotronic IGZO transistor. (b) Equivalent circuit diagram of the pressure sensor. (c) Output voltage of integrated TENG component. (d) Transfer characteristics of IGZO transistor with air dielectrics under different pressures. (e) Transfer characteristics of tribotronic IGZO transistor with air dielectrics under different pressures with same TENG displacement  $D = 0.07$  mm. (f) Output characteristics of tribotronic IGZO transistor under different TENG displacements. (g) The sensitivity of pressure sensor under different TENG displacements. (h) Real-time measurement for the pressure sensor. (i) Extracted response time.

photoresist AZ5214 to form the air gap. The TENG component can be integrated with the top gate via the extended gate electrode to drive/modulate the air-dielectric IGZO transistor (Fig. 3a, corresponding circuit diagram is in Fig. 3b). Notably, the integrated TENG component with high impedance is capable to pair the air-dielectric transistor with low capacitance and deliver sufficiently high  $V_{TENG}$  ( $-100$  to  $100$  V) to gate the device (Fig. 3c). Fig. 3d displays the pressure dependent transfer characteristics ( $I_D$  vs.  $V$ ) of the air-dielectric IGZO transistor. With the applied pressures increased from 55.5 to 344.4 kPa,  $I_D$  shows an increment tendency with  $V_G$  sweeping from  $-100$ – $100$  V at  $V_D$  of 15 V. Similarly, the tribotronic transfer characteristics in Fig. 3e shows an increment tendency with  $D$  increased from  $-0.07$ – $0.07$  mm under the same  $V_D$  of 15 V. Fig. 3f shows the corresponding output performance of tribotronic IGZO transistor via air dielectrics layer at a selected TENG displacement of 0.07 mm. The current level shows a distinct increment under  $F$  applied from 55.5 to 344.4 kPa, with  $I_D$  increasing from 1.9 to 3.2 nA at  $V_D$  of 15 V. To evaluate the sensitivity of the pressure sensor, Fig. 3g plots the curves of  $(I_D-I_0)/I_0$  versus applied pressures under different displacement states. Interestingly, the sensitivity defined as

$(I_D-I_0)/I_0/F$  (i.e., the slope of the curves) is dependent on  $D$ , which means the TENG displacement can be readily controlled to acquire different sensing properties on demand. This result demonstrates the tribotronic air-gap transistor can work as a tunable pressure sensor derived by external mechanical actions. To check the reliability, real-time pressure sensing under  $D = 0.07$  mm is shown in Fig. 3h.  $I_D$  represents a steady step-by-step increment with applied pressure from 55.5 to 248 kPa. The extracted response time is 120 ms in Fig. 3i. The demonstrated air-dielectric IGZO transistor powered by triboelectric potential offers an effective solution to tunable or multifunctional pressure/tactile sensors.

The tribotronic dual-gate IGZO transistor based versatile sensory platform is also applicable to be a tunable optical sensor due to the readily increased electrons density in IGZO under light illumination, [59] which is donated by the ionized oxygen vacancies. [60] The coupled triboelectric potential is assumed to be capable of modulating the photo responsivity by influencing the charge carrier density in IGZO channel. We firstly test the transfer characteristics of the dual-gate IGZO transistor under light illumination with light emitting diodes (LEDs) in

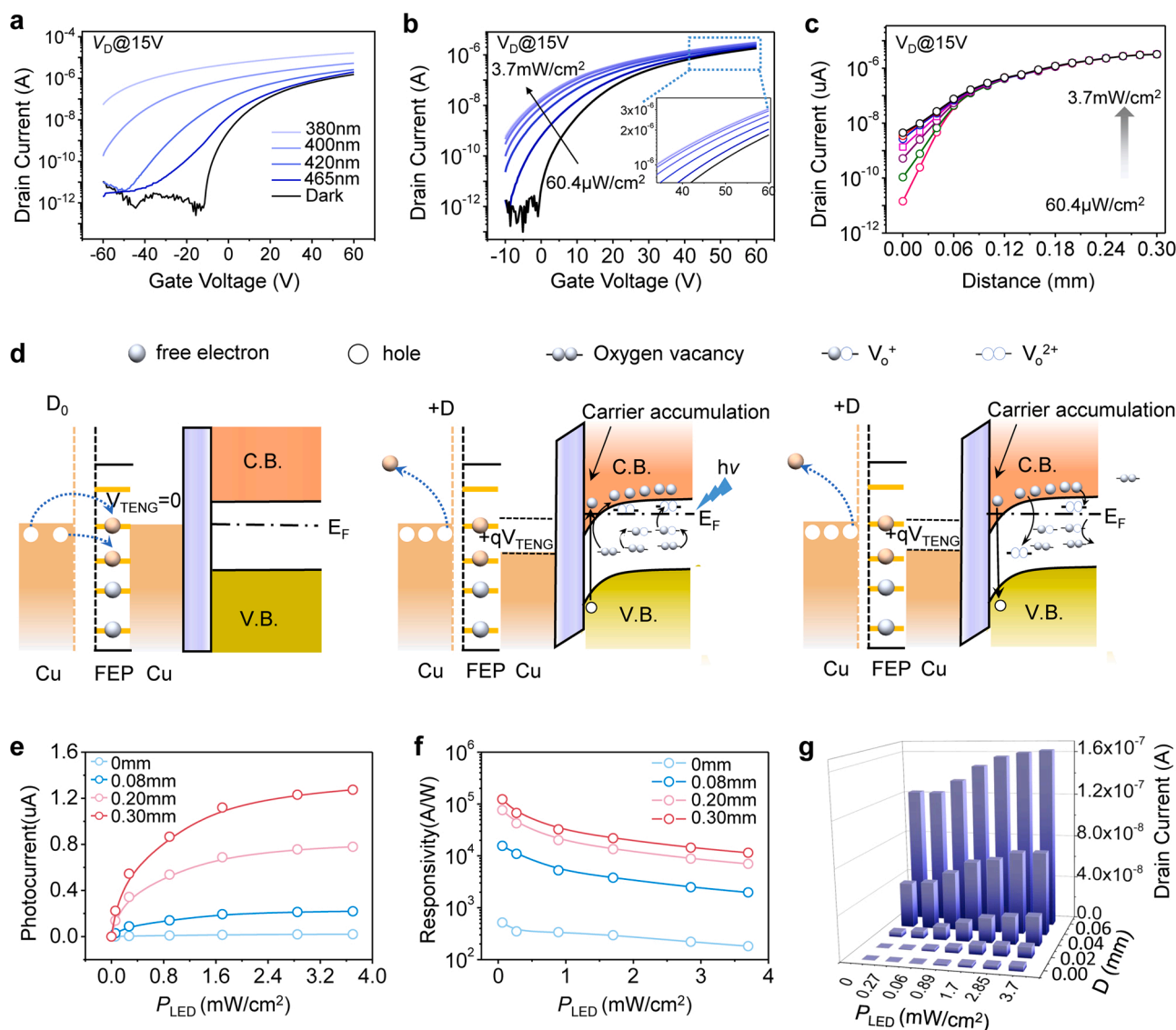


Fig. 4. Optical sensor based on tribotronic IGZO transistor. (a) Transfer characteristics of IGZO transistor under light illumination in different wavelength from 380 to 465 nm. (b) Transfer characteristic of IGZO transistor under different  $P_{light}$ s from  $60.4 \mu W/cm^2$  to  $3.7 mW/cm^2$  at  $V_D = 15$  V. (c) Transfer characteristics of tribotronic IGZO transistor under different  $P_{light}$ s. (d) Working mechanism of optical sensor based on tribotronic IGZO. (e) The photocurrent of IGZO transistor under different TENG displacements. (f) The responsibility to incident light power under different TENG displacements. (g) Drain current change under different  $P_{light}$ s and different TENG displacements.

different wavelength ( $\lambda = 380, 400, 420,$  and  $465$  nm, respectively). Under the same light intensity, the transfer curve under light illumination at  $\lambda = 380$  nm shows the largest increment compared with that in dark state (Fig. 4a). The drastically increased current can be attributed to the ionized-oxygen-deficiency donating electrons and intrinsic electrons excitation in IGZO channel. The light-induced  $V_T$  shift to the negative direction is related with the increased density of oxygen vacancies and photo-generated electrons, which make the applied gate bias lose its control on the transfer characteristics. Accordingly, we reasonably select the longer wavelength of  $465$  nm to illuminate the IGZO transistor (to achieve transfer curve with proper on/off ratio) to investigate the following photodetection properties. As shown in Fig. 4b, the transfer curve gradually shifts to the negative  $V_G$  direction with a decreased current on/off ratio under the light illumination ( $\lambda = 465$  nm) in different light intensities ( $P_{\text{light}} = 0.06, 0.27, 0.89, 1.7, 2.85,$  and  $3.7$   $\text{mW}\cdot\text{cm}^{-2}$ , respectively). The decreased on/off ratio also indicates that  $I_D$  responds more sensitive to the illuminated light at lower  $V_G$  ( $I_D$  increases from  $3.4$  pA to  $20$  nA at  $V_G = 0$  V) and less sensitive at higher  $V_G$  ( $I_D$  increases from  $1.8$  to  $3.08$   $\mu\text{A}$  at  $V_G = 60$  V). This is because smaller  $V_G$  induces limited electrons in IGZO channel, which gives more space for the photogenerated charge carriers to dominate the transport properties. This result means the photo response of IGZO transistor is closely related with  $V_G$ . For the tribotronic dual-gate IGZO transistor, as  $V_G$  can be readily replaced by triboelectric potential, corresponding photo response will be related with the TENG displacement  $D$ . As shown in the transfer curves of tribotronic IGZO transistor ( $I_D$  versus  $D$ ) under different  $P_{\text{light}}$ s (Fig. 4c),  $I_D$  increases with the increased  $D$  and increased  $P_{\text{light}}$ , respectively. The current variation trend is similar with that in Fig. 4b, i.e.,  $I_D$  is more sensitive at smaller  $D$  (displaying larger variation range of  $I_D$ ). Fig. 4d proposes the working mechanism of the triboelectric potential tuned optical sensor based on the tribotronic IGZO transistor. At the initial state with preset displacement  $D_0$  (an electrostatic equilibrium state between two friction layers with  $V_{\text{TENG}} = 0$  V), no triboelectric potential is applied to the device and IGZO channel is in flat-band state. When the mobile Cu electrode approaches FEP/Cu friction layer ( $D_+$  state), a positive triboelectric potential ( $+V_{\text{TENG}}$ ) is coupled to the device and accumulate electrons in IGZO channel. The energy band of IGZO is bent downward and electrons will dominate the transport properties. Under light illumination, the electrons at top of the valence band of IGZO are excited to transit into the conduction band. Furthermore, light illumination can ionize the oxygen vacancies in IGZO channel and convert them from electrical neutral state into doubly-ionized donor state ( $\text{Vo}^+$  and  $\text{Vo}^{2+}$ ). The donated electrons can also transit to the conduction band of IGZO. Consequently, the drain current is further increased under light illumination. When the light is removed, photo-generated electrons transit back to the valence band and recombine with photo-generated holes. Meanwhile, the donated electrons by  $\text{Vo}^{2+}$  (or  $\text{Vo}^+$ ) will also transit back to the oxygen vacancies, which act as hole traps. As the holes are bound to  $\text{Vo}^{2+}$  (or  $\text{Vo}^+$ ) during the ionization process of oxygen vacancy by light illumination. The donated electrons in conduction band needs more activation energy and more time to overcome the energy barrier to recombine with the hole of  $\text{Vo}^{2+}$  ( $\text{Vo}^{2+} + 2e \rightarrow \text{Vo}^0$ ).

To further evaluate the photo sensitivity of the tunable light sensor, photocurrent is extracted and plotted versus  $P_{\text{light}}$  (Fig. 4e). It is found that photocurrent increases with the applied  $D$  and tends to reach saturation at higher  $P_{\text{light}}$ . The photo responsivity ( $R$ ) indicates the current response to the light density, which is defined as  $R = (I_{\text{light}} - I_{\text{dark}})/P_{\text{light}}$  ( $I_{\text{light}}$  is the drain current under light irradiation,  $I_{\text{dark}}$  is the current under dark state, and  $P_{\text{light}}$  is the irradiation light power). Fig. 4f shows the photo responsivity of tribotronic IGZO transistor based light sensor, which is measured to be  $10^5$  A/W under TENG displacement at  $0.3$  mm. To more clearly indicate the synergetic effect of  $D$  and  $P_{\text{light}}$  on  $I_D$ , Fig. 4g plots the relevant 3D-histogram that  $I_D$  increases with the increased  $D$  and  $P_{\text{light}}$  and reaches  $1.63 \times 10^7$  A under  $D = 0.08$  mm and  $P_{\text{light}} = 3.7$   $\text{mW}\cdot\text{cm}^{-2}$ . More real-time synergetic effects of  $D$  and  $P_{\text{light}}$

on  $I_D$  are shown in Fig. S6.

With the development of artificial synaptic, various semiconductor materials have been used as transistor channel, e.g., two-dimensional conjugated polymer, nanowires, tin oxide nanoparticles, and amorphous oxide semiconductors. It is facile to use specific characteristics of these materials to achieve typical synaptic plasticity and emulate complex neural behaviors, including metaplasticity and homeostatic plasticity, [61] satiety, and depression. [62] It is also available to achieve synaptic plasticity and pain perception to via electro-optical modulation. [63] Among the mentioned semiconductor materials, amorphous oxide semiconductors have an important property of persistent photoconductivity (PPC) due to the inevitable existence of oxygen vacancy, which means the current needs more time to decay. This is because of the slow recombination of excited electrons and ionized  $\text{Vo}^{2+}$ , which is similar with the behavior of neurotransmitters in biological synapse (inset of Fig. 5a). Therefore, the PPC characteristics are promising to emulate the photoreceptor and satisfy the requirements of light-stimulated synaptic devices. It is possible to emulate the biological synaptic behaviors via pulse light signals, including excitatory post-synaptic current (EPSC), paired-pulse facilitation (PPF), and short-term/long-term plasticity (STP/LTP). Fig. 5a shows the schematic illustration of the mechanical behavior derived artificial photonic synaptic based on the tribotronic IGZO transistors. The pulse light signal and drain current are defined as presynaptic input signal and post-synaptic output signal, respectively. The conductivity of the IGZO channel layer is defined as the synaptic weight ( $W$ ). The integrated TENG component is capable to drive/modulate the synaptic transistor. Fig. 5b shows the EPSC responses to different  $P_{\text{light}}$ s illuminated on the device (illumination time  $\sim 5$  s). With  $P_{\text{light}}$  increased from  $26.8$  to  $186.8$   $\mu\text{W}\cdot\text{cm}^{-2}$  at  $D = 0$  mm, the EPSC increases from  $147$  pA to  $1.12$  nA. This is because an increasing number of photogenerated carriers and ionized oxygen vacancy are excited in conduction band of IGZO and leads to the increment of EPSC under stronger light illumination (also extracted as shown in Fig. S7a). Fig. 5c shows a typical PPF behavior under paired light pulses ( $P_{\text{light}} = 0.114$   $\text{mW}\cdot\text{cm}^{-2}$ , spike duration =  $5$  s, and interval time  $\Delta t_{\text{pre}} = 10$  s). The inset curve displays the PPF index, which is defined as  $A_2/A_1$  (where  $A_1$  and  $A_2$  are the EPSC amplitudes of first and second spikes, respectively), decreases from  $1.41$  to  $1.33$  with the increased  $\Delta t_{\text{pre}}$  from  $0.2$  to  $10$  s. Fig. 5d shows the EPSCs upon  $20$  light pulses ( $\Delta t_{\text{pre}} = 2$  s, spike duration =  $5$  s) in different  $P_{\text{light}}$ s. With  $P_{\text{light}}$  increased from  $0.06, 0.11,$  to  $0.18$   $\text{mW}\cdot\text{cm}^{-2}$ , the maximum EPSC reaches  $43$  pA,  $3.5$  nA and  $3.7$  nA, respectively. The influences of different light pulse intervals on EPSC are shown in Fig. S7b. Different numbers of light pulses can also significantly influence the amplitude of EPSC as shown in Fig. 5e, which increases from  $3$  to  $7.68$  nA under light pulse numbers from  $10$  to  $30$  with  $P_{\text{light}} = 0.27$   $\text{mW}\cdot\text{cm}^{-2}$ . The decay time extracted from a typical EPSC behavior is estimated to be  $\sim 10$  s with stretched exponential model (Fig. S8a), which belongs to STP region. With increased light pulse numbers, the STP to LTP transition can be achieved by repeated "stimulation" training.[64] As estimated in Fig. S8b, with EPSC triggered by different number of light pulses (spike duration =  $5$  s,  $\Delta t_{\text{pre}} = 2$  s,  $P_{\text{light}} = 0.27$   $\text{mW}\cdot\text{cm}^{-2}$ ), the simulated retention time is  $37.05, 58.7,$  and  $75.4$  s, respectively. It belongs to LTP region. Fig. 5f indicates the  $A_n/A_1$  (the ratio between the maximum conductance value and minimum conductance value) under illumination of light pulse in different numbers ( $10$ – $30$ ), with  $A_{30}/A_1$  reaching the maximum of  $12.267$ . The continuous light pulse illumination can lead to enhanced synaptic plasticity and has great potential in image recognition assisted with machine learning.

Based on the capability of emulating the characteristics of biological synapses, the artificial photonic synapse is used to perform the simulation of image edge detection. Generally, image edge detection is conducted through gradient information change, filtering, enhancement, detection, location, and positioning. We have designed  $3 \times 3$  matrix of artificial photonic synapses based on the tribotronic IGZO transistors,

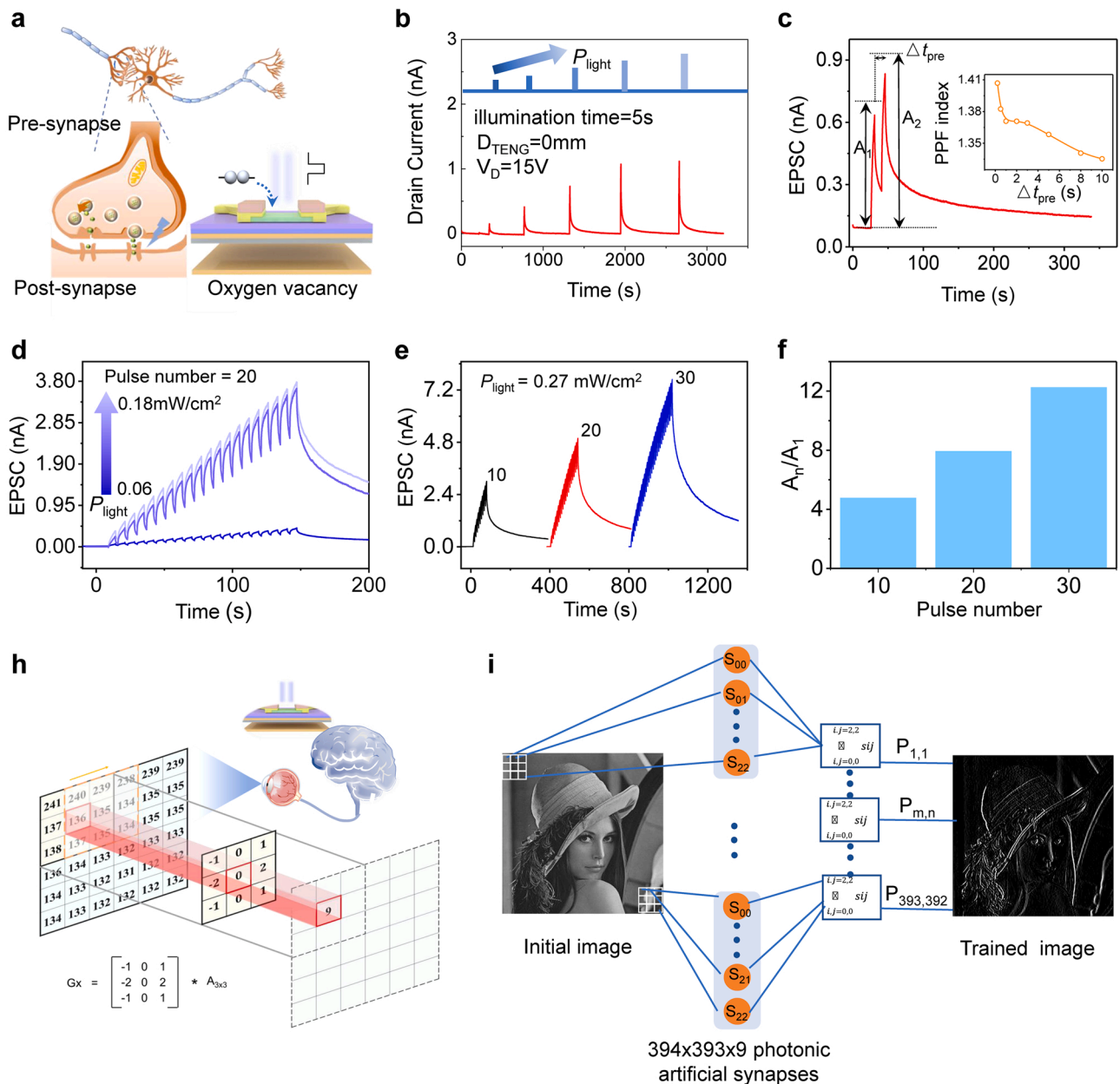


**Fig. 5.** Artificial photonic synaptic based on tribotronic IGZO transistor. (a) Schematic of the artificial photonic synaptic based on tribotronic IGZO transistor. (b) The EPSC responses to different  $P_{light}$ s under light pulse with  $V_D = 15$  V and  $D = 0$  mm. (c) The EPSC response activated by a pair of light pulses ( $P_{light} = 0.114$  mW-cm<sup>-2</sup>,  $\Delta t_{pre} = 10$  s,  $D = 0$  mm). The inset curve shows PPF index plotted as an exponential function of interval time between two sequential spikes. (d) multiple light-stimulated EPSC at different  $P_{light}$ s (pulse number = 20, pulse width = 5 s,  $P_{light} = 60.4$   $\mu$ W cm<sup>-2</sup>,  $P_{light} = 0.06, 0.11,$  and  $0.18$  mW cm<sup>-2</sup>,  $D = 0$  mm). (e) EPSC at different numbers of light pulse ( $P_{light} = 0.27$  mW-cm<sup>-2</sup>, pulse width = 5 s, pulse number = 10, 20, and 30,  $D = 0$  mm). (f) The current gain (defined as the ratio of  $A_n/A_1$ ) with different pulse numbers. (g) The working process of image edge detection based on the artificial photonic synapse. (h) The image edge detection along transverse direction of the selected image.

which can be regarded as Sobel operator to achieve image edge detection in transverse direction as shown in Fig. 5h. Each of  $3 \times 3$  gray color can be read from the image and convolved with the Sobel operator to obtain the transverse edge of the image. The input gray value in each pixel of the image can be reflected by the transconductance of IGZO photonic synaptic transistor gated by triboelectric potentials (i.e., equivalent  $V_{GS}$ ). The achieved  $I_D$  in tribotronic transistors under different  $P_{light}$ s illumination can be regarded as the synaptic weights (i.e., the channel conductance). Then we can use  $394 \times 393 \times 9$  photonic synapses (either synapse is coordinated as  $S_{ij}$ , representing the device in row  $i$  and column  $j$ ) to detect image edge along transverse direction (Fig. 5i). The  $394 \times 393$  pixels of image are convolutedly processed by adopting  $394 \times 393 \times 9$  photonic synapses to acquire the trained

image. Fig. S9 also successfully demonstrates the result of other image edge detections at vertical direction, transverse and vertical direction, and transverse or vertical direction, respectively. The performed image edge detection with the artificial photonic synapses based on tribotronic dual-gate IGZO transistor is of great significance in image analyzing, covering various applications such as corner detection, feature extraction, machine vision, etc.

### 3. Conclusion

In summary, we demonstrate a versatile sensory platform (including distance/pressure/optical sensor and artificial photonic synapse) based on triboelectric potential tuned IGZO transistor. The distance sensor

shows a high sensitivity of  $15.73 \times 10^5 \text{ mm}^{-1}$  in large displacement region (0.16–0.3 mm); the pressure sensor can response to small pressures ranging and possess short response time ( $\sim 120$  ms); the combined optical sensor represents a high responsivity of  $10^5 \text{ A/W}$ . Moreover, according to the oxygen-deficiency-related persistent photocurrent characteristics, the versatile sensory device can be used as an artificial photonic synapse assisted with triboelectric potential modulation to imitate typical biological synaptic behaviors and to implement image edge detection. The triboelectric potential tuned IGZO transistor realizes synergetic pressure/optical sensing upon mechanical displacement modulation (or triboelectric potential modulation), which is highly promising in low-power multifunctional sensors, electronic skin, image recognition/treatment and neuromorphic computation.

## 4. Experiments

### 4.1. Materials preparation

PDMS mold (Sylgard 184, Dow Corning) was prepared by mixing the silicon elastomer base and curing agent (10:1 wt ratio). After mixing uniformly using a glass rod, the mixture was placed in a vacuum box to remove bubbles. Then, the base and curing agent mixtures were poured on a Si wafer with required microstructure (here is convex strip) in the drying box at  $70^\circ\text{C}$  for 3 h for solidification. After peeling off the microstructured PDMS mold, Cr/Au electrode was patterned on the PDMS assisted with photo mask by thermal evaporation. We use sol-gel process to prepare IGZO channel with 0.1 M solution of IGZO precursors in 2-Methoxyethanol (molar ratio of In:Ga:Zn = 9:1:2). We dissolved 225.6 mg of  $\text{In}(\text{NO}_3)_3 \cdot x\text{H}_2\text{O}$ , 21.3 mg of  $\text{Ga}(\text{NO}_3)_3 \cdot x\text{H}_2\text{O}$  and 31.5 mg of  $\text{Zn}(\text{NO}_3)_2 \cdot x\text{H}_2\text{O}$  in 10 ml 2-Methoxyethanol solvent. The solution was then stirred for 12 h at  $75^\circ\text{C}$ . After treating the  $\text{SiO}_2/\text{Si}$  wafer substrate by UV ozone cleaning for 15 min, the well-mixed precursor solution was spin-coated (4000 rpm, 30 s) on it after filtration by using  $0.2 \mu\text{m}$  disposable filters. Finally, the IGZO semiconductor film was annealed at  $100^\circ\text{C}$  for 1 min to remove the solvent followed with another annealing process at  $350^\circ\text{C}$  for 1 h under air conduction.

### 4.2. Device fabrication

$\text{SiO}_2/\text{Si}$  wafer (n-type doped Si wafer with 300 nm  $\text{SiO}_2$  layer) was served as the substrate, which was also used as the bottom gate. First, IGZO solution is spin-coated on the substrate and patterned to define the channel via photolithography (photoresist AZ5214) and wet etching process. Second, Cr/Au source-drain electrodes (10/40 nm) were prepared on the substrate through a standard lift-off process. Third, photoresist (AZ5214) is patterned on the electrodes and used as the spacer. Finally, TENG component is integrated as a bottom gate at the bottom of  $\text{SiO}_2/\text{Si}$  wafer to drive/tune the IGZO transistor, while the PDMS mold is laminated on top to achieve the air-dielectric device as a pressure sensor.

### 4.3. Characterizations

The precise displacements of TENG were controlled by a linear motor and the output properties were measured by using Keithley 6514 system electrometer. The electrical performance of the transistor was characterized with a semiconductor device analyzer (Agilent B1500A) with a probe station under ambient environment. During the test, the device and the TENG should be well electrostatically screened to protect the test system from the disturbance of surrounding electrostatic charges.

### 4.4. Edge detection simulation

Edge detection is an essential problem in image processing and computer vision. Herein, we simulate an edge detection process based on the tribotronic IGZO transistors. Sobel (x and y gradient) operator is

adopted to detect the edge of the image.

Sobel operator along transverse direction is denoted as:

$$\begin{bmatrix} -1 & 0 & 1 \\ -2 & 0 & 2 \\ -1 & 0 & 1 \end{bmatrix}$$

Sobel operator along vertical direction is denoted as:

$$\begin{bmatrix} -1 & -2 & -1 \\ 0 & 0 & 0 \\ 1 & 2 & 1 \end{bmatrix}$$

In our device, the input gray value in each pixel of the image can be reflected by the transconductance of IGZO photonic synaptic transistor. That is, nine IGZO photonic synaptic transistors with different transconductance can constitute a Sobel operator to achieve image edge detection. Each pixel in the convolved image can be generated by the dot product of the 9-dimensional voltage vector mapped from a  $3 \times 3$  input original image and the 9-dimensional conductance vector mapped from a  $3 \times 3$  convolution matrix. The calculation formula of edge detection along transverse direction is given below:

$$G_x = \begin{bmatrix} -1 & 0 & 1 \\ -2 & 0 & 2 \\ -1 & 0 & 1 \end{bmatrix} * A_{3 \times 3}$$

Among them,  $G_x$  is the convolved gray value (i.e., the  $I_D$  in our device);  $A_{3 \times 3}$  is the voltage vector mapped from a  $3 \times 3$  input original image, just as shown in Fig. 5h. The  $394 \times 393$  pixels of image are convolutedly processed by adopting  $394 \times 393 \times 9$  photonic synapses to acquire the trained image. Similarly, the tribotronic IGZO transistor based edge detection along vertical direction can be simulated (Fig. 5i and Fig. S9).

## Declaration of Competing Interest

The authors declare that they have no known competing financial interests or personal relationships that could have appeared to influence the work reported in this paper.

## Acknowledgements

This work is financially supported by the National Key Research and Development Program of China (2016YFA0202703), the National Natural Science Foundation of China (52073031), the Fundamental Research Funds for the Central Universities (E0EG6801X2), Beijing Nova Program (Z191100001119047), the ‘‘Hundred Talents Program’’ of the Chinese Academy of Sciences.

## Appendix A. Supporting information

Supplementary data associated with this article can be found in the online version at doi:10.1016/j.nanoen.2021.106617.

## References

- [1] A. Chortos, J. Liu, Z. Bao, Pursuing prosthetic electronic skin, *Nat. Mater.* 15 (2016) 937–950.
- [2] G. Schwartz, B.C. Tee, J. Mei, A.L. Appleton, D.H. Kim, H. Wang, Z. Bao, Flexible polymer transistors with high pressure sensitivity for application in electronic skin and health monitoring, *Nat. Commun.* 4 (2013) 1859.
- [3] S. Lee, A. Reuveny, J. Reeder, S. Lee, H. Jin, Q. Liu, T. Yokota, T. Sekitani, T. Isoyama, Y. Abe, Z. Suo, T. Someya, A transparent bending-insensitive pressure sensor, *Nat. Nanotechnol.* 11 (2016) 472–478.
- [4] J. Wang, Y. Chen, L.-A. Kong, Y. Fu, Y. Gao, J. Sun, Deep-ultraviolet-triggered neuromorphic functions in In-Zn-O phototransistors, *Appl. Phys. Lett.* 113 (2018), 151101.
- [5] J. Sun, Y. Fu, Q. Wan, Organic synaptic devices for neuromorphic systems, *J. Phys. D: Appl. Phys.* 51 (2018), 314004.
- [6] Y. Kim, A. Chortos, W. Xu, Y. Liu, J.Y. Oh, D. Son, J. Kang, A.M. Foudeh, C. Zhu, Y. Lee, S. Niu, J. Liu, R. Pfattner, Z. Bao, T.W. Lee, A bioinspired flexible organic artificial afferent nerve, *Science* 360 (2018) 998–1003.

- [7] K. Takei, T. Takahashi, J.C. Ho, H. Ko, A.G. Gillies, P.W. Leu, R.S. Fearing, A. Javey, Nanowire active-matrix circuitry for low-voltage macroscale artificial skin, *Nat. Mater.* 9 (2010) 821–826.
- [8] C. Qian, J. Sun, L.-a Kong, Y. Fu, Y. Chen, J. Wang, S. Wang, H. Xie, H. Huang, J. Yang, Y. Gao, Multilevel nonvolatile organic photomemory based on vanadyl-phthalocyanine/para-sexiphenyl heterojunctions, *ACS Photon.* 4 (2017) 2573–2579.
- [9] C. Qian, L.-a Kong, J. Yang, Y. Gao, J. Sun, Multi-gate organic neuron transistors for spatiotemporal information processing, *Appl. Phys. Lett.* 110 (2017), 083302.
- [10] L.-a Kong, J. Sun, C. Qian, Y. Fu, J. Wang, J. Yang, Y. Gao, Long-term synaptic plasticity simulated in ionic liquid/polymer hybrid electrolyte gated organic transistors, *Org. Electron.* 47 (2017) 126–132.
- [11] L.-a Kong, J. Sun, C. Qian, C. Wang, J. Yang, Y. Gao, Spatially-correlated neuron transistors with ion-gel gating for brain-inspired applications, *Org. Electron.* 44 (2017) 25–31.
- [12] S. Lee, S. Franklin, F.A. Hassani, T. Yokota, M.O.G. Nayeem, Y. Wang, R. Leib, G. Cheng, D.W. Franklin, T. Someya, Nanomesh pressure sensor for monitoring finger manipulation without sensory interference, *Science* 370 (2020) 966–970.
- [13] Q. Zhang, T. Jiang, D. Ho, S. Qin, X. Yang, J.H. Cho, Q. Sun, Z.L. Wang, Transparent and self-powered multistage sensation matrix for mechanosensation application, *ACS Nano* 12 (2018) 254–262.
- [14] J.H. Lee, K.Y. Lee, M.K. Gupta, T.Y. Kim, D.Y. Lee, J. Oh, C. Ryu, W.J. Yoo, C. Y. Kang, S.J. Yoon, J.B. Yoo, S.W. Kim, Highly stretchable piezoelectric-pyroelectric hybrid nanogenerator, *Adv. Mater.* 26 (2014) 765–769.
- [15] X. Liu, P. Cui, J. Wang, W. Shang, S. Zhang, J. Guo, G. Gu, B. Zhang, G. Cheng, Z. Du, A robust all-inorganic hybrid energy harvester for synergistic energy collection from sunlight and raindrops, *Nanotechnology* 32 (2021), 075401.
- [16] M. Kaltenbrunner, M.S. White, E.D. Glowacki, T. Sekitani, T. Someya, N. S. Sariciftci, S. Bauer, Ultrathin and lightweight organic solar cells with high flexibility, *Nat. Commun.* 3 (2012) 770.
- [17] Z.L. Wang, Entropy theory of distributed energy for internet of things, *Nano Energy* 58 (2019) 669–672.
- [18] H. Qin, G. Gu, W. Shang, H. Luo, W. Zhang, P. Cui, B. Zhang, J. Guo, G. Cheng, Z. Du, A universal and passive power management circuit with high efficiency for pulsed triboelectric nanogenerator, *Nano Energy* 68 (2020), 104372.
- [19] Y. Zi, H. Guo, Z. Wen, M.H. Yeh, C. Hu, Z.L. Wang, Harvesting low-frequency (<5 Hz) irregular mechanical energy: a possible killer application of triboelectric nanogenerator, *ACS Nano* 10 (2016) 4797–4805.
- [20] J.R. Huang, X.X. Yang, J.R. Yu, J. Han, C.K. Jia, M. Ding, J. Sun, X.L. Cao, Q.J. Sun, Z.L. Wang, A universal and arbitrary tactile interactive system based on self-powered optical communication, *Nano Energy* 69 (2020), 104419.
- [21] F.-R. Fan, Z.-Q. Tian, Z. Lin Wang, Flexible triboelectric generator, *Nano Energy* 1 (2012) 328–334.
- [22] Z.L. Wang, On Maxwell's displacement current for energy and sensors: the origin of nanogenerators, *Mater. Today* 20 (2017) 74–82.
- [23] J. Han, C. Xu, J. Zhang, N. Xu, Y. Xiong, X. Cao, Y. Liang, L. Zheng, J. Sun, J. Zhai, Q. Sun, Z.L. Wang, Multifunctional coaxial energy fiber toward energy harvesting, storage, and utilization, *ACS Nano* 15 (2021) 1597–1607.
- [24] Y.J. Yang, J. Han, J.R. Huang, J. Sun, Z.L. Wang, S. Seo, Q.J. Sun, Stretchable energy-harvesting tactile interactive interface with liquid-metal-nanoparticle-based electrodes, *Adv. Funct. Mater.* 30 (2020), 1909652.
- [25] S. Qin, Q. Zhang, X. Yang, M. Liu, Q. Sun, Z.L. Wang, Hybrid piezo/triboelectric-driven self-charging electrochromic supercapacitor power package, *Adv. Energy Mater.* 8 (2018), 1800069.
- [26] J. Cheng, W. Ding, Y. Zi, Y. Lu, L. Ji, F. Liu, C. Wu, Z.L. Wang, Triboelectric microplasma powered by mechanical stimuli, *Nat. Commun.* 9 (2018) 3733.
- [27] H. Zhang, J. Yu, X. Yang, G. Gao, S. Qin, J. Sun, M. Ding, C. Jia, Q. Sun, Z.L. Wang, Ion gel capacitively coupled tribotronic gating for multiparameter distance sensing, *ACS Nano* 14 (2020) 3461–3468.
- [28] J. Guo, G. Cheng, Z. Du, The recent progress of triboelectric nanogenerator-assisted photodetectors, *Nanotechnology* 31 (2020), 292003.
- [29] M. Zheng, S. Lin, L. Xu, L. Zhu, Z.L. Wang, Scanning probing of the tribovoltaic effect at the sliding interface of two semiconductors, *Adv. Mater.* 32 (2020), e2000928.
- [30] G. Gao, J. Yu, X. Yang, Y. Pang, J. Zhao, C. Pan, Q. Sun, Z.L. Wang, Tribotronic transistor of MoS<sub>2</sub>, *Adv. Mater.* 31 (2019), 1806905.
- [31] C. Zhang, W. Tang, L. Zhang, C. Han, Z.L. Wang, Contact electrification field-effect transistor, *ACS Nano* 8 (2014) 8702–8709.
- [32] G. Gao, B. Wan, X. Liu, Q. Sun, X. Yang, L. Wang, C. Pan, Z.L. Wang, Tunable tribotronic dual-gate logic devices based on 2D MoS<sub>2</sub> and black phosphorus, *Adv. Mater.* 30 (2018), e1705088.
- [33] Y. Chen, G. Gao, J. Zhao, H. Zhang, J. Yu, X. Yang, Q. Zhang, W. Zhang, S. Xu, J. Sun, Y. Meng, Q. Sun, Piezotronic graphene artificial sensory synapse, *Adv. Funct. Mater.* 29 (2019), 1900959.
- [34] X.X. Yang, J.R. Yu, J. Zhao, Y.H. Chen, G.Y. Gao, Y.F. Wang, Q.J. Sun, Z.L. Wang, Mechanoplastic tribotronic floating-gate neuromorphic transistor, *Adv. Funct. Mater.* 30 (2020), 2002506.
- [35] J. Yu, S. Qin, H. Zhang, Y. Wei, X. Zhu, Y. Yang, Q. Sun, Fiber-shaped triboiontronic electrochemical transistor, *Research* 2021 (2021), 9840918.
- [36] Y. Meng, J. Zhao, X. Yang, C. Zhao, S. Qin, J.H. Cho, C. Zhang, Q. Sun, Z.L. Wang, Mechanosensation-active matrix based on direct-contact tribotronic planar graphene transistor array, *ACS Nano* 12 (2018) 9381–9389.
- [37] X. Yang, J. Han, J. Yu, Y. Chen, H. Zhang, M. Ding, C. Jia, J. Sun, Q. Sun, Z. L. Wang, Versatile triboiontronic transistor via proton conductor, *ACS Nano* 14 (2020) 8668–8677.
- [38] H. Kang, C. Zhao, J. Huang, D.H. Ho, Y.T. Megra, J.W. Suk, J. Sun, Z.L. Wang, Q. Sun, J.H. Cho, Fingerprint-inspired conducting hierarchical wrinkles for energy-harvesting E-skin, *Adv. Funct. Mater.* 29 (2019), 1903580.
- [39] J. Yu, X. Yang, G. Gao, Y. Xiong, Y. Wang, J. Han, Y. Chen, H. Zhang, Q. Sun, Z. L. Wang, Bioinspired mechano-phonic artificial synapse based on graphene/MoS<sub>2</sub> heterostructure, *Sci. Adv.* 7 (2021) eabd9117.
- [40] J.; Yu, G.; Gao, J.; Huang, X.; Yang, J.; Han, H.; Zhang, Y.; Chen, C.; Zhao, Q.; Sun, Z.L. Wang, Contact-electrification-activated artificial afferents at femtojoule energy, *Nat. Commun.* 12 (2021) 1581.
- [41] S.C. Mannsfeld, B.C. Tee, R.M. Stoltenberg, C.V. Chen, S. Barman, B.V. Muir, A. N. Sokolov, C. Reese, Z. Bao, Highly sensitive flexible pressure sensors with microstructured rubber dielectric layers, *Nat. Mater.* 9 (2010) 859–864.
- [42] Y.-C. Huang, Y. Liu, C. Ma, H.-C. Cheng, Q. He, H. Wu, C. Wang, C.-Y. Lin, Y. Huang, X. Duan, Sensitive pressure sensors based on conductive microstructured air-gap gates and two-dimensional semiconductor transistors, *Nat. Electron.* 3 (2020) 59–69.
- [43] J. Jang, H. Kim, S. Ji, H.J. Kim, M.S. Kang, T.S. Kim, J.E. Won, J.H. Lee, J. Cheon, K. Kang, W.B. Im, J.U. Park, Mechanoluminescent, air-dielectric MoS<sub>2</sub> transistors as active-matrix pressure sensors for wide detection ranges from footsteps to cellular motions, *Nano Lett.* 20 (2020) 66–74.
- [44] S. Ji, J. Jang, J.C. Hwang, Y. Lee, J.H. Lee, J.U. Park, Amorphous oxide semiconductor transistors with air dielectrics for transparent and wearable pressure sensor arrays, *Adv. Mater. Technol.* 5 (2019), 1900928.
- [45] S.H. Shin, S. Ji, S. Choi, K.H. Pyo, B. Wan An, J.; Park, J.; Kim, J.Y.; Kim, K.S.; Lee, S.Y.; Kwon, J.; Heo, B.G.; Park, J.U. Park, Integrated arrays of air-dielectric graphene transistors as transparent active-matrix pressure sensors for wide pressure ranges, *Nat. Commun.* 8 (2017) 14950.
- [46] Y. Zang, F. Zhang, D. Huang, X. Gao, C.A. Di, D. Zhu, Flexible suspended gate organic thin-film transistors for ultra-sensitive pressure detection, *Nat. Commun.* 6 (2015) 6269.
- [47] Q. Sun, D.H. Kim, S.S. Park, N.Y. Lee, Y. Zhang, J.H. Lee, K. Cho, J.H. Cho, Transparent, low-power pressure sensor matrix based on coplanar-gate graphene transistors, *Adv. Mater.* 26 (2014) 4735–4740.
- [48] Q. Sun, W. Seung, B.J. Kim, S. Seo, S.W. Kim, J.H. Cho, Active matrix electronic skin strain sensor based on piezopotential-powered graphene transistors, *Adv. Mater.* 27 (2015) 3411–3417.
- [49] D.H. Ho, Q. Sun, S.Y. Kim, J.T. Han, D.H. Kim, J.H. Cho, Stretchable and multimodal all graphene electronic skin, *Adv. Mater.* 28 (2016) 2601–2608.
- [50] R. Pfattner, A.M. Foudeh, S. Chen, W. Niu, J.R. Matthews, M. He, Z. Bao, Dual-gate organic field-effect transistor for pH sensors with tunable sensitivity, *Adv. Electron. Mater.* 5 (2019), 1800381.
- [51] O. Lopez-Sanchez, D. Lembke, M. Kayci, A. Radenovic, A. Kis, Ultrasensitive photodetectors based on monolayer MoS<sub>2</sub>, *Nat. Nanotechnol.* 8 (2013) 497–501.
- [52] H. Chen, W. Zhang, M. Li, G. He, X. Guo, Interface engineering in organic field-effect transistors: principles, applications, and perspectives, *Chem. Rev.* 120 (2020) 2879–2949.
- [53] C.A. Di, Y. Liu, G. Yu, D. Zhu, Interface engineering: an effective approach toward high-performance organic field-effect transistors, *Acc. Chem. Res.* 42 (2009) 1573–1583.
- [54] Y. Choi, Q. Sun, E. Hwang, Y. Lee, S. Lee, J.H. Cho, On-demand doping of graphene by stamping with a chemically functionalized rubber lens, *ACS Nano* 9 (2015) 4354–4361.
- [55] X. Yang, G. Hu, G. Gao, X. Chen, J. Sun, B. Wan, Q. Zhang, S. Qin, W. Zhang, C. Pan, Q. Sun, Z.L. Wang, Coupled ion-gel channel-width gating and piezotronic interface gating in ZnO nanowire devices, *Adv. Funct. Mater.* 29 (2019), 1807837.
- [56] C. Peng, W. Jiang, Y. Li, X. Li, J. Zhang, Photoelectric IGZO electric-double-layer transparent artificial synapses for emotional state simulation, *ACS Appl. Electron. Mater.* 1 (2019) 2406–2414.
- [57] J. Sun, S. Oh, Y. Choi, S. Seo, M.J. Oh, M. Lee, W.B. Lee, P.J. Yoo, J.H. Cho, J.-H. Park, Optoelectronic synapse based on IGZO-alkylated graphene oxide hybrid structure, *Adv. Funct. Mater.* 28 (2018), 1804397.
- [58] K. Nomura, H. Ohta, A. Takagi, T. Kamiya, M. Hirano, H. Hosono, Room-temperature fabrication of transparent flexible thin-film transistors using amorphous oxide semiconductors, *Nature* 432 (2004) 488–492.
- [59] X. Yu, T.J. Marks, A. Facchetti, Metal oxides for optoelectronic applications, *Nat. Mater.* 15 (2016) 383–396.
- [60] B. Ryu, H.-K. Noh, E.-A. Choi, K.J. Chang, O-vacancy as the origin of negative bias illumination stress instability in amorphous In–Ga–Zn–O thin film transistors, *Appl. Phys. Lett.* 97 (2010), 022108.
- [61] H. Han, F. Ge, M. Ma, H. Yu, H. Wei, X. Zhao, H. Yao, J. Gong, L. Qiu, W. Xu, Mixed receptors of AMPA and NMDA emulated using a "Polka Dot"-structured two-dimensional conjugated polymer-based artificial synapse, *Nanoscale Horiz.* 5 (2020) 1324–1331.
- [62] S. Zhang, K. Guo, H. Han, H. Yu, H. Wei, J. Gong, W. Xu, Multiplexed neurotransmission emulated by a p–n cross nanowire transistor for satiety, depression, and drug withdrawal, *Adv. Funct. Mater.* 31 (2021), 2101917.
- [63] H. Wei, Y. Ni, L. Sun, H. Yu, J. Gong, Y. Du, M. Ma, H. Han, W. Xu, Flexible electro-optical neuromorphic transistors with tunable synaptic plasticity and nociceptive behavior, *Nano Energy* 81 (2020), 105648.
- [64] Z.Q. Wang, H.Y. Xu, X.H. Li, H. Yu, Y.C. Liu, X.J. Zhu, Synaptic learning and memory functions achieved using oxygen ion migration/diffusion in an amorphous InGaZnO memristor, *Adv. Funct. Mater.* 22 (2012) 2759–2765.